

An Electronically Tunable, First-Order Fabry-Perot Infrared Filter

10 April 1995

Prepared by

J. T. Knudtson, D. S. Levy, and K. C. Herr
Space and Environment Technology Center
Technology Operations

Prepared for

SPACE AND MISSILE SYSTEMS CENTER
AIR FORCE MATERIEL COMMAND
2430 E. El Segundo Boulevard
Los Angeles Air Force Base, CA 90245

Programs Group

19950607 019


APPROVED FOR PUBLIC RELEASE;
DISTRIBUTION UNLIMITED

DTIC QUALITY INSPECTED 5

This report was submitted by The Aerospace Corporation, El Segundo, CA 90245-4691, under Contract No. F04701-93-C-0094 with the Space and Missile Systems Center, 2430 E. El Segundo Blvd., Los Angeles Air Force Base, CA 90245. It was reviewed and approved for The Aerospace Corporation by A. B. Christensen, Principal Director, Space and Environment Technology Center.

This report has been reviewed by the Public Affairs Office (PAS) and is releasable to the National Technical Information Service (NTIS). At NTIS, it will be available to the general public, including foreign nationals.

This technical report has been reviewed and is approved for publication. Publication of this report does not constitute Air Force approval of the report's findings or conclusions. It is published only for the exchange and stimulation of ideas.



Donald R. Gasner
SMC/XRX

REPORT DOCUMENTATION PAGE			Form Approved OMB No. 0704-0188	
Public reporting burden for this collection of information is estimated to average 1 hour per response, including the time for reviewing instructions, searching existing data sources, gathering and maintaining the data needed, and completing and reviewing the collection of information. Send comments regarding this burden estimate or any other aspect of this collection of information, including suggestions for reducing this burden to Washington Headquarters Services, Directorate for Information Operations and Reports, 1215 Jefferson Davis Highway, Suite 1204, Arlington, VA 22202-4302, and to the Office of Management and Budget, Paperwork Reduction Project (0704-0188), Washington, DC 20503.				
1. AGENCY USE ONLY (Leave blank)		2. REPORT DATE 10 April 1995		3. REPORT TYPE AND DATES COVERED
4. TITLE AND SUBTITLE An Electronically Tunable, First-Order Fabry-Perot Infrared Filter			5. FUNDING NUMBERS F04701-93-C-0094	
6. AUTHOR(S) J. T. Knudtson, D. S. Levy, and K. C. Herr				
7. PERFORMING ORGANIZATION NAME(S) AND ADDRESS(ES) The Aerospace Corporation Technology Operations El Segundo, CA 90245-4691			8. PERFORMING ORGANIZATION REPORT NUMBER TR-92(2013)-2	
9. SPONSORING/MONITORING AGENCY NAME(S) AND ADDRESS(ES) Space and Missile Systems Center Air Force Materiel Command 2430 E. El Segundo Boulevard Los Angeles Air Force Base, CA 90245			10. SPONSORING/MONITORING AGENCY REPORT NUMBER SMC-TR-95-17	
11. SUPPLEMENTARY NOTES				
12a. DISTRIBUTION/AVAILABILITY STATEMENT Approved for public release; distribution unlimited			12b. DISTRIBUTION CODE	
13. ABSTRACT (Maximum 200 words) A tunable infrared filter capable of scanning from 8.2 to 12.8 μm has been designed, constructed and tested. It is a first-order Fabry-Perot interferometer with piezoelectrically driven cavity spacing. Multilayer dielectric coatings for the partially transmitting mirrors were designed to minimize the wavelength-dependent phase change produced by reflection. The transmission bandwidth ranged from 2.8 to 4.0% across the tuning range. Continuous scanning at 20 Hz rates was demonstrated.				
14. SUBJECT TERMS Tunable infrared filter, Fabry-Perot, First-order Fabry Perot			15. NUMBER OF PAGES 31	
			16. PRICE CODE	
17. SECURITY CLASSIFICATION OF REPORT UNCLASSIFIED	18. SECURITY CLASSIFICATION OF THIS PAGE UNCLASSIFIED	19. SECURITY CLASSIFICATION OF ABSTRACT UNCLASSIFIED	20. LIMITATION OF ABSTRACT	

Contents

1. Introduction	1
2. Reflective Coatings	3
3. The Fabry-Perot Interferometer	7
4. FPI Transmission Spectra	9
5. Peak Wavelength and FPI Spacing	11
6. Wavelength-Dependent Phase Change and Tuning Range	13
7. Transmission Bandwidth	17
8. Wavelength Stability	19
9. Scanning and Dithering Capability	21
10. Three-Micron Region Operation	23
11. Summary	25
References	27

Figures

1. Measured and calculated reflectance for the coating	5
2. The FPI transmission at four different cavity spacings.	10
3. The measured FPI peak wavelength as a function of cavity spacing	11
4. The fractional phase change as a function of peak wavelength.	13
5. The peak wavelength versus cavity spacing for different orders.	15
6. The transmission bandwidth as a function of wavelength	18
7. The FPI transmission in the 3- μ m region at two cavity spacings.	23

<input checked="" type="checkbox"/>
<input type="checkbox"/>
<input type="checkbox"/>

Distribution /	
Availability Codes	
Dist	Avail and/or Special
A-1	

1. Introduction

Our remote sensing projects in the longwave infrared (8–12 μm band) frequently require bandpass filters that overlap molecular absorption/emission bands. Because custom filters are relatively expensive (\$5–15K), we depend on finding an appropriate filter from manufacturer's surplus stock. Frequently, the filters we obtain are not optimally matched to the desired molecular band. We have also used circularly variable, wavelength-tunable filters, but they have narrow rectangular slits (<1 mm) that place significant constraints on the optical systems in which they can be used. We have developed an electronically tunable filter that can replace sets of fixed wavelength filters or be continuously scanned. In addition, its ability to rapidly change the transmitted wavelength offers a new capability for rapid wavelength-modulated detection or spectral dithering.

The filter is a scanning Fabry–Perot Interferometer (FPI) operated in first order. Although first-order (and low-order) FPIs are the basis for fixed-wavelength interference filters, and high-order ($n > 100$) scanning FPIs are commercially available, we are unaware of any reports of a scanning first-order FPI.¹

For collimated, normally incident input radiation, the transmission peaks of an FPI occur when the cavity spacing between the two mirrors, ℓ , is an integral number, n , of half wavelengths, λ .²

$$\ell = \frac{n\lambda}{2} \quad (1)$$

For a first-order FPI, the cavity length is simply one-half the desired wavelength. Therefore, to tune the FPI transmission peak from 8–12 μm , the cavity spacing must be scanned from 4–6 μm .

We need to be concerned about other order peaks falling in the 8–12 μm tuning range. The wavelength of any other order, λ_n , can be calculated for a given ℓ by rearranging Eq. (1).

$$\lambda_n = \frac{2\ell}{n} \quad (2)$$

Equation (2) shows that as the cavity length scans 4–6 μm , the second-order peak will scan from 4–6 μm . This is well outside our 8–12 μm tuning range and can be efficiently eliminated with an 8–12 μm bandpass filter in the optical system. Orders higher than $n = 2$ correspond to even shorter wavelengths and are also eliminated by the 8–12 μm filter. In general, the region over which a first-order FPI can be tuned without overlapping another order is just one-half the longest wavelength in the desired tuning range. In our case, the maximum wavelength is 12 μm , and the tuning range is 6 μm (from 12–6 μm).

2. Reflective Coatings

The full-width at half-height (the bandwidth) of the FPI's transmission peak depends on the reflectance of the partially reflecting mirrors (R), and the FPI order (n). Higher reflectance and higher order decrease the bandwidth. The bandwidth, in percent of the center wavelength, $\Delta\lambda/\lambda$ (%), is given by Eq. (3).

$$\frac{\Delta\lambda}{\lambda} (\%) = \frac{100}{nN_R} \quad (3)$$

N_R is the reflective finesse, which is proportional to the reflectance and is given by Eq. (4).

$$N_R = \frac{\pi\sqrt{R}}{1 - R} \quad (4)$$

The bandwidth is a strongly dependent function of the reflectance. For instance, a reflectance of 0.90 corresponds to a bandwidth of 3.3%. If the reflectance drops 5% to 0.85, the bandwidth increases to 5.2% (a 58% increase). Since most mirrors will have some variation in reflectance across the tuning range, there will be a corresponding variation in bandwidth across the tuning range.

Because of their simplicity, we first investigated metallic thin-film mirrors. A partially transmitting mirror was made by coating 115 Å of gold on a ZnSe substrate. The measured reflectance and transmittance of the gold-coated surface were 0.89 and 0.012, respectively, at 10.0 μ. The reflectance was measured with a reflectance accessory in an FTIR relative to a freshly coated gold mirror. Therefore, the loss due to absorption (or scattering) was 0.098.

A low-order FPI was assembled from two of the gold-coated mirrors. The measured transmittance of the FPI at 10.0 μm was very low, 0.01. The expected FPI transmission can be calculated from Eq. (5), where T_m is the transmission of the mirror and τ is the transmittance of the FPI.³

$$\tau = \frac{T_m^2}{(1 - R)^2} \quad (5)$$

Based on the measured mirror transmittance and reflectance, the calculated FPI transmission is 0.015, in reasonable agreement with the 0.01 measured value. Although partially reflecting gold mirrors are broadband and inexpensive, their absorptance severely reduces the FPI throughput.

Multilayer dielectric reflectors with high reflectance and low absorption were investigated. They consist of alternating layers of high and low index material.⁴ Each layer is one-quarter of a wavelength thick. The light reflected from successive boundaries is in phase and recombines construc-

tively. A high/low index pair is called a quarter-wave stack, and the thickness is one-quarter of the design wavelength.

A quarter-wave stack is also reflective at wavelengths near the design wavelength. The width of the reflective region around the design wavelength increases nonlinearly with the ratio of the refractive indices of the two materials.⁴ In order to maximize the width of the reflective region, we chose Ge($n = 4.1$) as the high index material. Both ZnS($n = 2.15$) and ThF₄($n = 1.35$) were candidates for the low index material.

The phase change of the reflected wave in a quarter-wave stack is 180° at the design wavelength. At other wavelengths, the phase change varies from 180° . This has several significant effects on the performance of the FPI, which will be described below. Our coating design sought to minimize this wavelength-dependent phase by keeping the number of quarter-wave stacks as low as possible.

With these initial conditions, we selected the following design:

$$\text{ZnSe substrate/Ge/Ge/ZnS/Ge/ZnS/Ge,} \quad (6)$$

where the optical thickness of each layer was one-quarter of the $10.0\text{-}\mu$ design wavelength. The two Ge layers adjacent to the substrate are referred to as “absentee layers” since they have very little effect on the reflectance at the design wavelength. However, they do increase the width of the reflective region.⁴

The calculated reflectance of the multilayer stack in Eq. (6) is shown in Fig. 1. The reflectance was calculated with a commercial program that used the matrix method from Reference 4. In the $8\text{--}13\text{ }\mu\text{m}$ region, there are two maxima: at $8.8\text{ }\mu$, $R = 0.887$ and at $11.6\text{ }\mu$, $R = 0.893$. At $10.0\text{ }\mu$, the design wavelength, $R = 0.870$.

The reflectance data in Fig 1 can be used with Eq. (3) to calculate the FPI’s bandwidths. At the reflectance maximum ($R = 0.893$), the bandwidth is 3.60%. The reflectance changes most rapidly with wavelength on the short-wavelength side of the reflective region. At $8.2\text{ }\mu$, $R = 0.855$, and the bandwidth would be 4.98%. On the long-wavelength side, $R = 0.858$ at $13.0\text{ }\mu$, corresponding to a bandwidth of 4.88%. Therefore, over the $8.2\text{--}13.0\text{ }\mu$ wavelength range, the bandwidth varies by a factor of 1.4 (maximum/minimum).

The reflectance of a mirror fabricated to design specifications in Eq. (6) is also shown in Fig. 1. The reflectance was measured in an FTIR (2 cm^{-1} resolution) with a reflectance accessory relative to a gold-coated mirror ($R = 0.99$). The reflectance is in good agreement with the calculated value at $10\text{ }\mu$. At both longer and shorter wavelengths, the reflectance is several percent below the calculated value. The deviation from the calculated reflectance is 0.039 at $8.2\text{ }\mu$ and 0.011 at $13.0\text{ }\mu$.

The deviations in the reflectance from the design values is probably due to small variations in the Ge coating thickness. The coating vendor monitored the Ge coating thickness by measuring the transmission at $\lambda \approx 1.0\text{ }\mu$ through a microscope slide adjacent to the mirror substrate. The absorption of

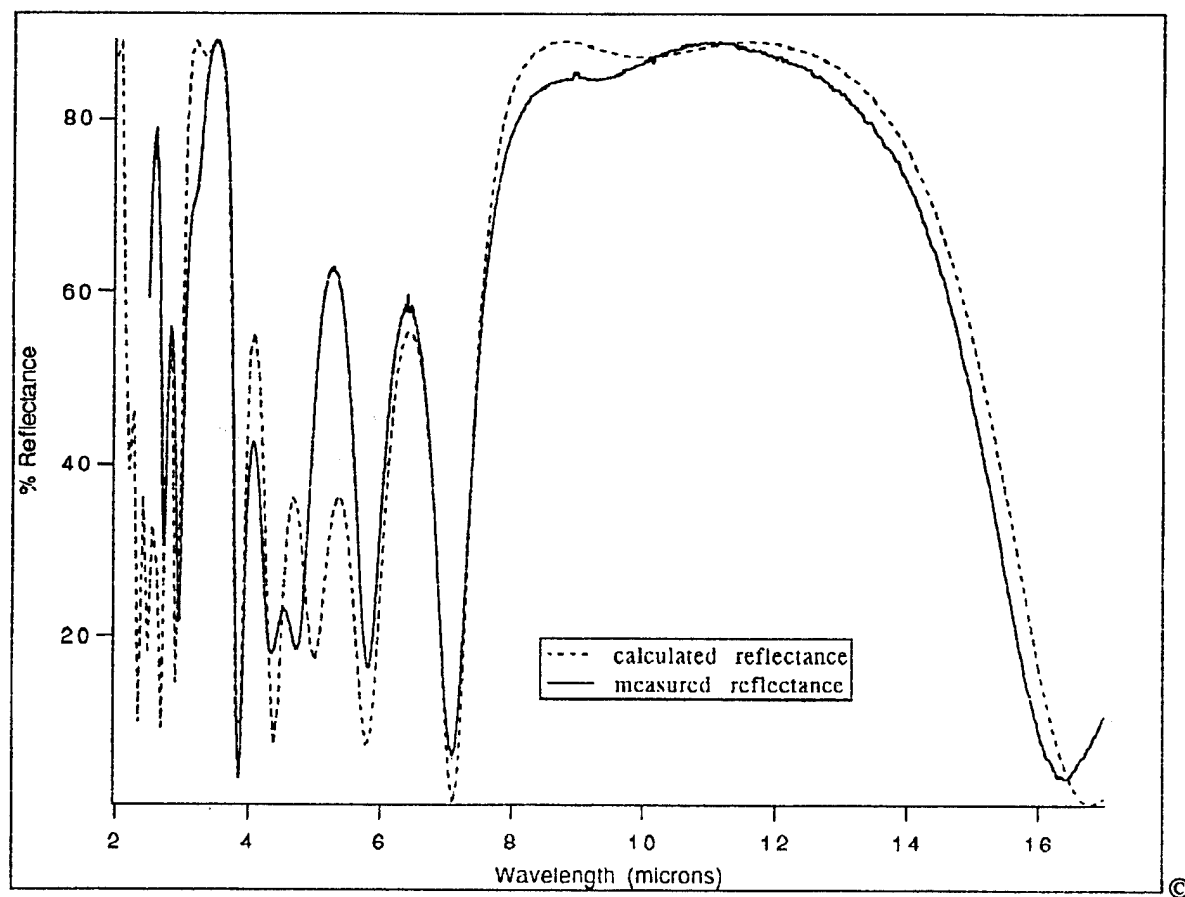


Figure 1. Measured and calculated reflectance for the coating: substrate GeGeZnSGeZnSGe.

Ge at $1\ \mu\text{m}$ is sufficiently strong that several microscope slides were required for each Ge layer. This process probably increased the error in measuring the Ge layer thickness. Shifting the optical monitoring wavelength to longer wavelengths ($> 2\ \mu$) should eliminate this problem.

3. The Fabry-Perot Interferometer

A tunable, first-order FPI was assembled using a Burleigh Instruments TL-38IR piezoelectric drive unit. The TL-38IR can scan up to $7\text{ }\mu\text{m}$ using the RC-44 ramp generator (0–1000 V). A special jig was constructed to align the mirrors and adjust their spacing. The transmitted interferogram produced by a $1.3\text{ }\mu\text{m}$ diode-pumped YAG laser was monitored while the mirrors were epoxied in place. A PbS vidicon camera was used to image the transmitted beam. The absorption by the Ge significantly attenuated the transmitted beam. The etalon was assembled in a clean hood to minimize the effects of contamination. Several attempts were required to obtain the first-order spacing ($5\text{ }\mu$).

The mirror substrates were 1.5-in.-diameter, 1-cm-thick ZeSe. The substrates were polished to $\lambda/20$ ($\lambda = 0.63\text{ }\mu$) on the mirror side and $\lambda/10$ on the back side. They were wedged 0.5° . At $8\text{ }\mu\text{m}$, the front surfaces are flat to $\lambda/250$. Assuming the deviation from flatness is spherical, the flatness finesse is approximately 125 (uncoated). This is sufficient to maintain the reflective finesse (about 30). The backside of the mirrors were also coated with a broadband antireflective coating.

4. FPI Transmission Spectra

Figure 2 shows the transmission of the FPI at four different spacings. When the transmitted peak is at 8.5 μm and 9.9 μm , the transmission is about 80%. At 11 μm , the transmission starts to decrease, and at 12.1 μm , it is 50%.

The acceptance angle of the FPI is sufficiently large that the $f/4.5$ conical FTIR beam should have only a small effect on the transmission spectrum. To maintain the bandwidth to within 10%, the maximum angle of incidence, α , for the FPI depends on both the order and the reflective finesse as given in Eq. (7).³

$$\alpha \text{ (radians)} = \frac{1}{\sqrt{nN_R}} \quad (7)$$

For $N_R = 30$ and $n = 1$, α is 10.5° , which is more than adequate to accept the 6.4° maximum angle of incidence in the $f/4.5$ FTIR beam.

The wavelength dependence of the transmission maxima in Fig. 2 suggests absorption by something with increasing absorption in the 11–12.5 μm region. We have reviewed the absorption spectra of materials that could contribute to the transmission loss. GeO_2 has strong absorption centered at 11.6 μm , and it is sufficiently broad to account for the loss out to 13 μm .⁵ The GeO_2 could be produced by oxidation of the outer Ge layer of the FPI mirror. We can calculate the effect of absorption on the FPI transmission using Eq. (5) and equating the mirror transmission, T_m , with $1-R-A$, where A is the loss due to absorption (or scattering). For a typical reflectance of 0.87, absorption losses of 1, 2, 3, and 4% yield FPI transmissions of 0.85, 0.72, 0.59, and 0.48. Thus, a few percent absorption can account for the FPI transmission losses.

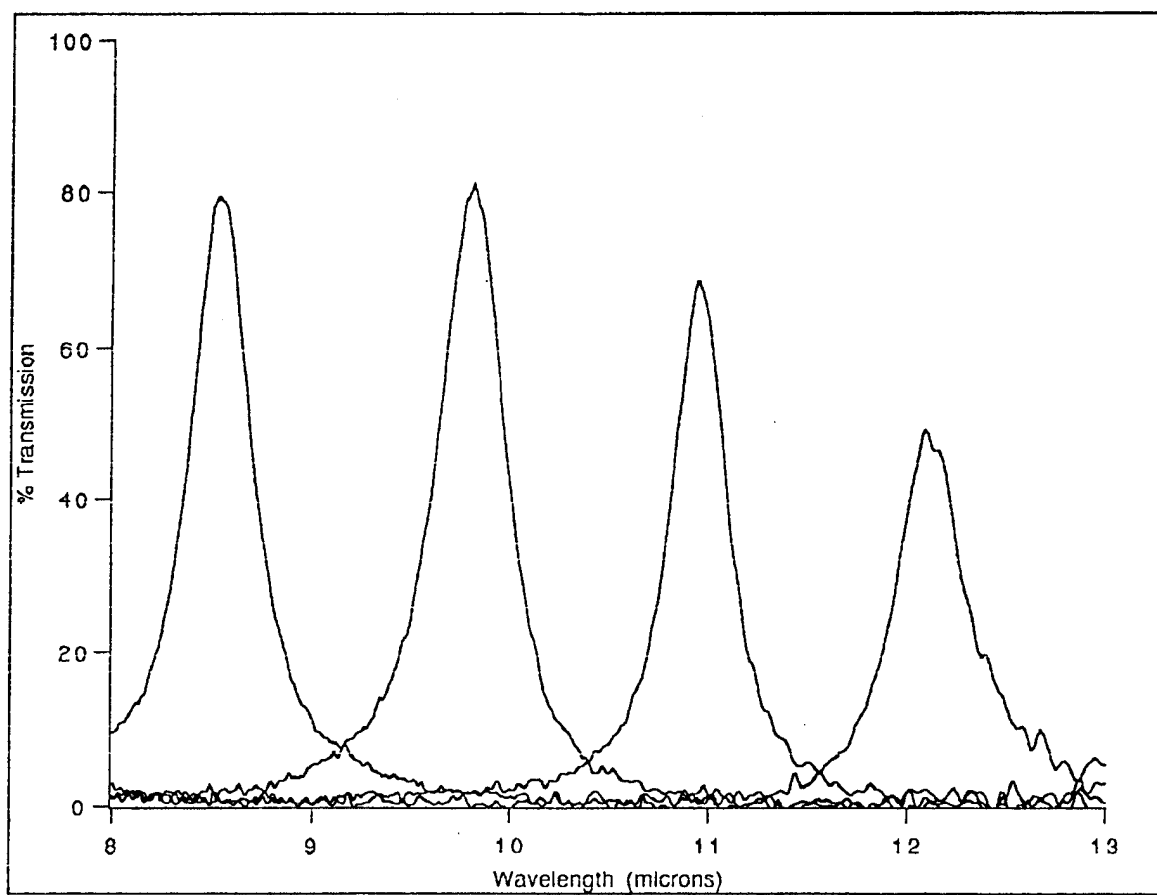


Figure 2. The FPI transmission at four different cavity spacings.

5. Peak Wavelength and FPI Spacing

In Fig. 3, the wavelength of the transmission peak, λ_{peak} , is plotted versus the FPI spacing. The solid black line in Fig. 3 has a slope of 2, which is the expected value for a first-order FPI [see Eq. (1)]. The difference between the expected and measured slopes is due to a wavelength-dependent reflective phase change in the multilayer dielectric coating.

The phase of the reflected wave from the multilayer dielectric mirror is 180° at the design wavelength ($10.0\ \mu\text{m}$). This is the phase change used to derive Eq. (1), which predicts that the FPI mirror spacing should be one-half the wavelength. In Fig. 3, we can see that the peak wavelength at $10\ \mu\text{m}$ occurs at a $5\text{-}\mu\text{m}$ spacing (to within a few tenths of a micron). However, at wavelengths shorter than $10\ \mu\text{m}$, the spacing is smaller than expected, and at wavelengths larger than $10\ \mu\text{m}$, the spacing is larger than expected. To scan the wavelength from 8 to $12\ \mu\text{m}$ now requires scanning the spacing from 3.3 to $6.3\ \mu\text{m}$; about one micron more than expected for a mirror with no wavelength-dependent phase change.

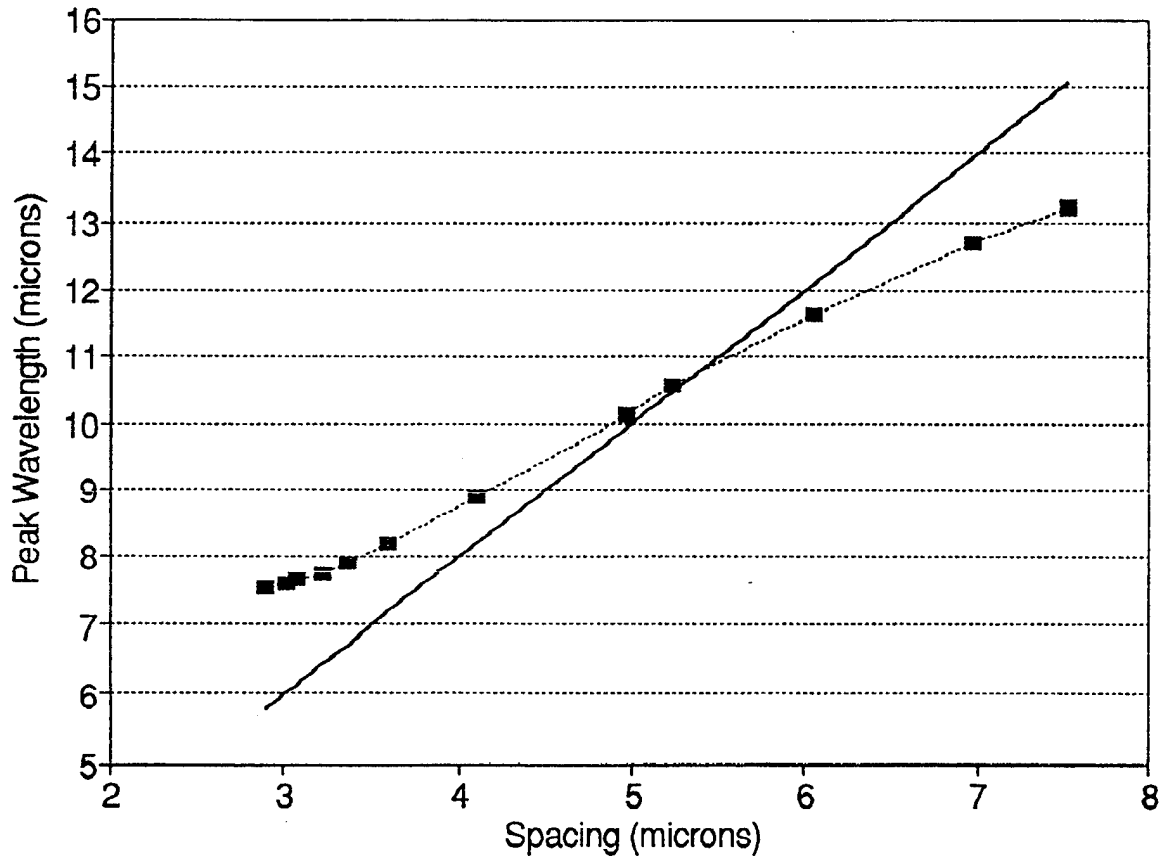


Figure 3. The measured FPI peak wavelength as a function of cavity spacing. The solid line is from Eq. (1) and has a slope of 2.0.

The data in Fig. 3 were taken with a spectral mirror set in which a stripe of the substrate was masked during the mirror coating process. At each FPI spacing, spectra were recorded of both the coated and uncoated portions of the mirror. The uncoated FPI spacing was calculated from the uncoated free spectral range (there is no wavelength-dependent phase change for the uncoated mirror). The spacing in the coated portion of the FPI is just the coated spacing minus twice the coating thickness.

The coating thickness was measured using a Sloan Dektak surface profiler. The thickness was measured at seven locations, and the average thickness was $3.71 \pm 0.44 \mu\text{m}$ (1σ). This is significantly smaller than the $4.82 \mu\text{m}$ calculated from the coating design using the indices of refraction for Ge and ZnS given earlier. The Dektak profiles showed the coated surface to be rough compared to the uncoated substrate. Surface bumps of $1\text{--}1.5 \mu\text{m}$ occurred frequently, and the average roughness (peak-to-peak) was approximately $0.5 \mu\text{m}$. The surface roughness contributes significantly to the error in measuring the coating thickness. In addition, the coating vendors previously described difficulty in producing the Ge layers, which may cause the actual coating thickness to differ from the calculated value. A third value for the coating thickness can be calculated by recalling that the reflected phase should be 180° at the design wavelength. This is equivalent to assuming that the cavity spacing is $5 \mu\text{m}$ when the transmitted peak wavelength is $10 \mu\text{m}$. This yields a coating thickness of $4.58 \mu\text{m}$. This is the value used for the data in Fig. 3.

6. Wavelength-Dependent Phase Change and Tuning Range

Atherton, Reay, and Ring have accounted for the wavelength-dependent phase change by adding a fractional, wavelength-dependent-order correction, $\epsilon\lambda$.³ This is the deviation (in radians) from the expected π radians phase change of the reflected wave. $\epsilon\lambda/\pi$, the fractional phase change, can be calculated from the striped mirror data using Eq. (8), where ℓ is the cavity spacing derived from the uncoated free spectral range, and λ is the transmission peak wavelength.

$$\frac{\epsilon\lambda}{\pi} = \frac{2\ell - \lambda}{\lambda} \quad (8)$$

In Fig. 4, $\epsilon\lambda/\pi$ is plotted versus the peak wavelength. Also shown is the phase change calculated from our thin-film program. They are in good agreement.

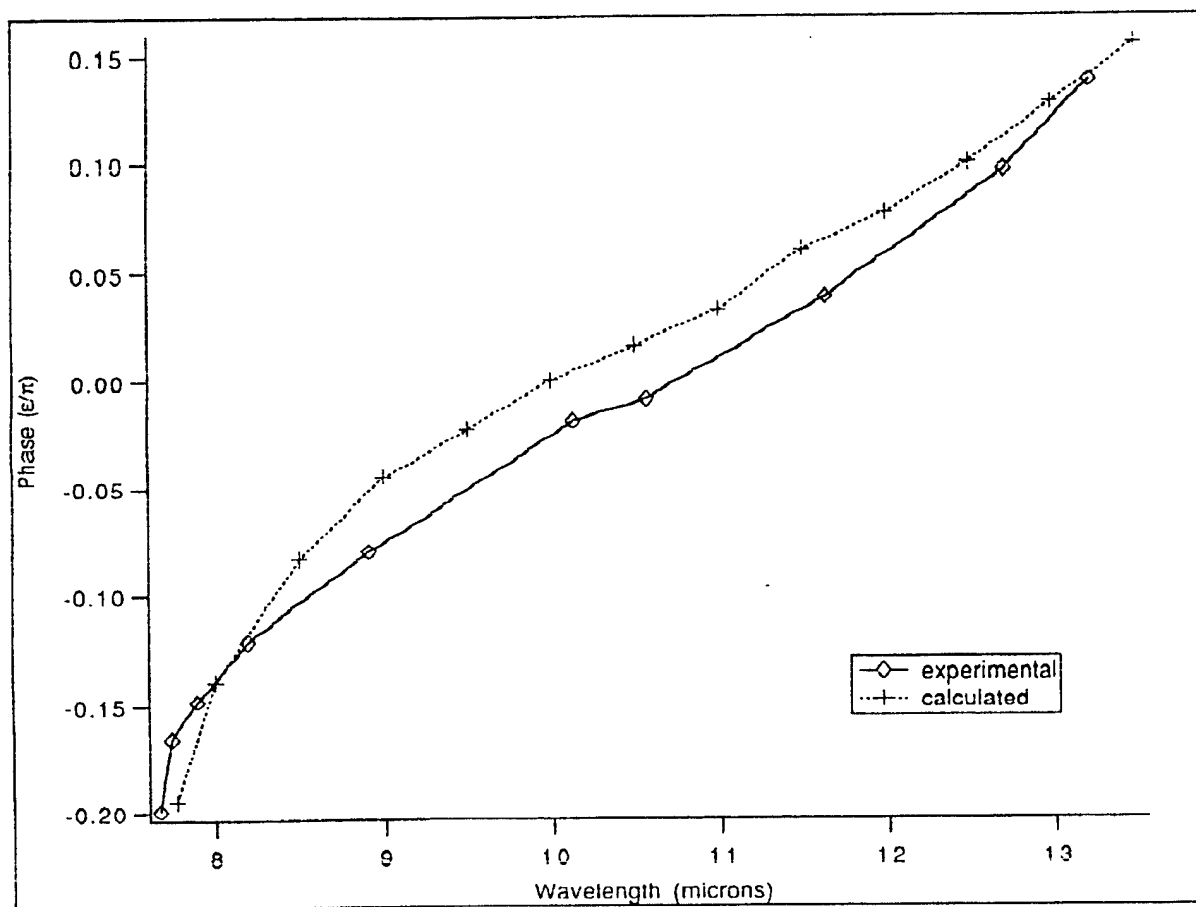


Figure 4. The fractional phase change as a function of peak wavelength.

The peak wavelength can now be calculated from the cavity spacing and the fractional phase change,

$$\lambda = \frac{2\ell}{n + \varepsilon_\lambda / \pi} . \quad (9)$$

Figure 5 shows a plot of the calculated peak wavelength versus cavity spacing for $n = 0, 1, 2$, and 3 . Figure 5 is useful for visualizing the FPI's tuning range. For instance, a first-order FPI tuned to a $12\text{-}\mu\text{m}$ transmission peak would almost transmit $7.3\text{ }\mu\text{m}$ radiation in second order. This is closer to our tuning range than the $6\text{-}\mu\text{m}$ predicted by Eq. (2), but it can still be effectively blocked with an $8\text{--}12\text{ }\mu\text{m}$ bandpass filter.

The zero-order transmission curve is of interest. For the coating design presented above, it occurs at a cavity spacing too small to be of interest. However, we have worked with another coating design that used 16 layers to produce a broad reflectance zone. The phase shifts for this design were quite large, even for wavelengths near the design wavelength. This caused the zero-order peaks to severely overlap the first-order peaks, and the tuning range was too small to be useful.

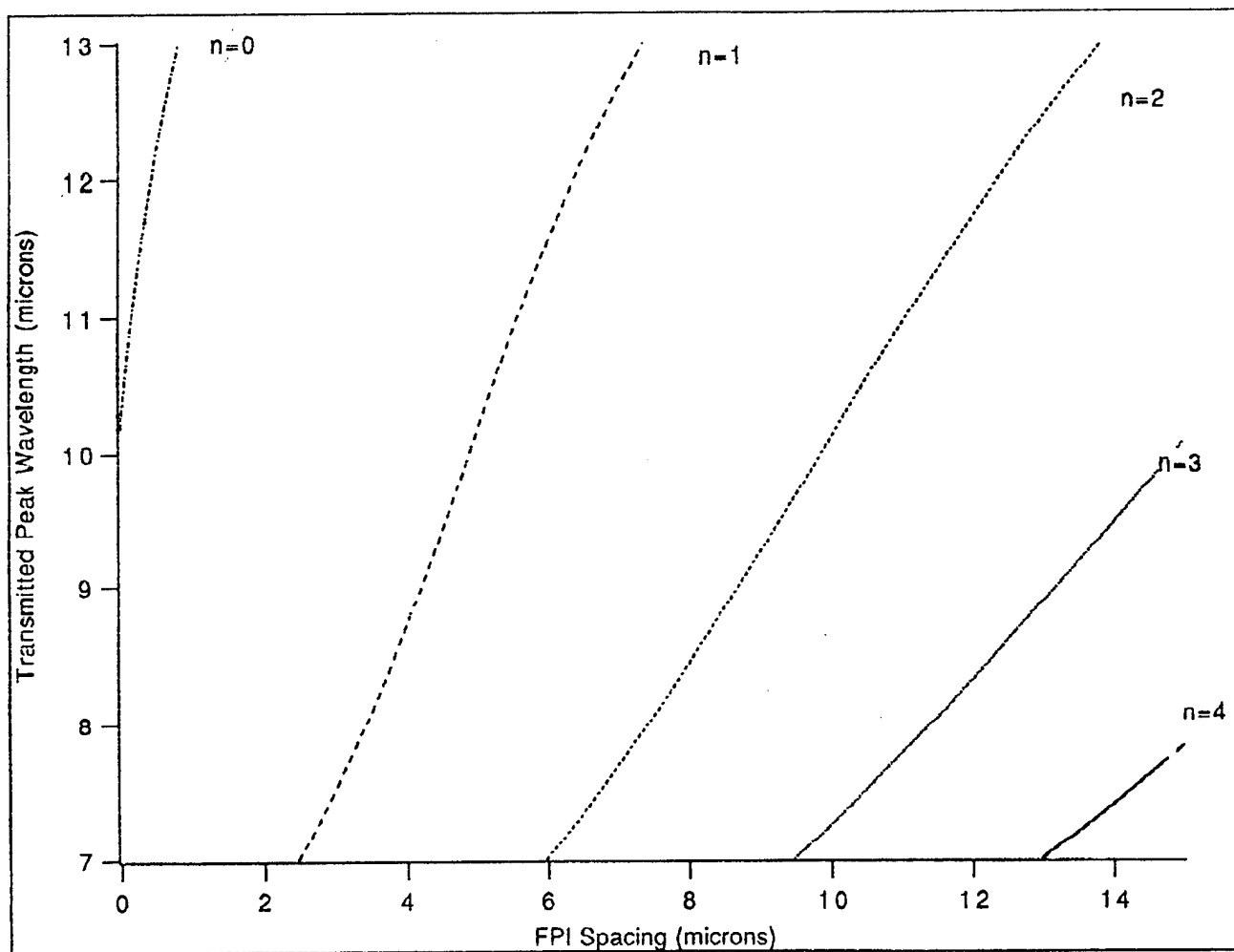


Figure 5. The peak wavelength versus cavity spacing for different orders.

7. Transmission Bandwidth

The wavelength-dependent phase change affects the transmission bandwidth. We expect the bandwidth to decrease as the reciprocal of the order [see Eq.(4)].

Atherton et al. have calculated the effect of the phase change on the bandwidth as given in Eq. (10)

$$\frac{\Delta\lambda(\%) }{\lambda} = \frac{1}{N_R \left(N + \frac{\varepsilon_\lambda}{\pi} + \frac{\lambda}{\pi} \frac{d\varepsilon_\lambda}{d\lambda} \right)}, \quad (10)$$

where

$$\frac{1}{\pi} \frac{d\varepsilon_\lambda}{d\lambda}$$

is the slope of the phase change versus wavelength plotted in Fig. 4, and N_R is the reflective finesse given in Eq. (3).³

The calculated bandwidth with the phase correction [Eq.(10)] and without the phase correction [Eq. (4)] are shown as a function of wavelength in Fig. 6. The effect of the phase correction is to reduce the bandwidth by about 1–2%, depending on wavelength. The bandwidth of the transmission peaks, measured in an FTIR, are also shown in Fig. 6. They are in good agreement with the widths calculated from Eq. (10) with some differences at the beginning and end of the tuning range. The measured bandwidths are probably too large at these points because the transmission does not return to the baseline. This causes the transmission passband to change shape and distort the bandwidth measurement.

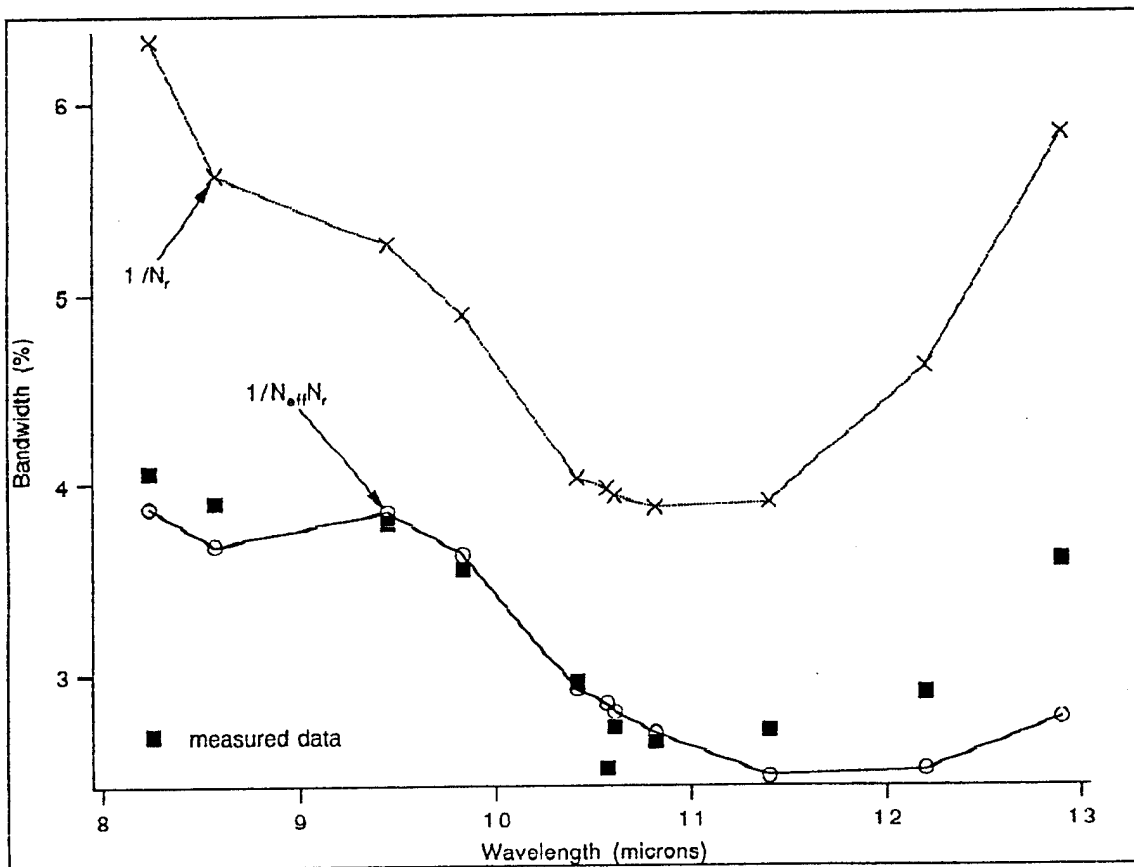


Figure 6. The transmission bandwidth as a function of wavelength. The (x) points are calculated based solely on reflectance (Eq. 3). The (O) points are calculated based on the fractional order model (Eq. 10). The (■) points are the measured bandwidths.

8. Wavelength Stability

The transmission peak was observed to drift between transmission measurements in the FTIR. The peak wavelength sometimes drifted a few percent (about one transmission peak width) overnight and infrequently over periods as short as several hours. This was probably due to room-temperature changes affecting the FPI cavity spacing.

The effect of temperature changes on the FPI can be calculated from the thermal expansion coefficient of the FPI and the change in transmitted peak wavelength with cavity spacing ($d\lambda/d\ell$). The cavity length of the TL-38IR changes 51 nm/C°. The slope of Fig. 3, $d\lambda/d\ell$, at 10 μm is 1.3. Therefore, the transmitted peak wavelength changes 0.066 μm per C°. At 10 μm , the full-bandwidth at half-height is 0.32 μm . Therefore, a temperature change of 2.3°C is sufficient to shift the peak wavelength one-half width, which reduces the transmission at the original wavelength by one-half.

The wavelength stability due to room -temperature fluctuation was significantly improved by a foam rubber jacket around the FPI body. For outdoor use (in a field-portable spectrometer), a thin-film heater is being designed to compensate for the larger thermal variations.

9. Scanning and Dithering Capability

The first-order FPI was operated in a continuous-scan mode in order to record emission spectra in the 8.2–12.8 μm region. A Burleigh RC-44 was used to generate a 0–1000 V sawtooth waveform. An $f/1.5$ ZnSe lens immediately behind the FPI focused the transmitted radiation on a 1-mm² HgCdTe infrared detector. The source was either a 900°K blackbody fitted with one of several possible narrowband infrared filters, or a line-tunable waveguide CO₂ laser. A series of four filters in the 8.2–12.8 μm region was used to calibrate the transmitted peak wavelength with sawtooth voltage.

The voltage-to-wavelength linearity was good up to 20 Hz scan rates. At faster rates, the FPI was unable to scan the full 8.2–12.8 μm region. The reduced scan was due to the dampening effects of air on the mirror scanning motion. An FPI was installed in a vacuum container, and scan rates of 100 Hz were observed.

The transmission bandwidth, while scanning, was measured with the CO₂ laser at 10.3 μm . The bandwidth was 3.2%, in good agreement with the bandwidth measured by the FTIR in the nonscanning mode, as shown in Fig. 6. The bandwidth measurements using the laser source were significantly more accurate and convenient than those using the blackbody/filter source. Since the bandwidths of the filters (1–3%) were comparable to the bandwidths of the FPI, the FPI bandwidth would have to be deconvoluted from the measured data.

The filter can tune smaller spectral intervals (i.e., 1 μm) at significantly higher rates. This is useful in some infrared radiometric situations where a narrowband molecular emission/absorption feature rides on top of a broadband (quasi-blackbody) background emission. The drive electronics can be modified to alternately tune filter wavelength to overlap the molecular feature and then to sample the background emission adjacent to the molecular feature. This spectral dithering produces a square-wave-modulated signal whose amplitude is proportional to the molecular emission radiance. It is essentially a rapid background subtraction technique.

The maximum rate of spectrally dithering depends on the size of the spectral interval. In one application where the filter dithered between 9.7–10.6 μm , the maximum rate was 100 Hz. For smaller spectral intervals, about 0.1 μm , we have been able to use the natural frequency of the piezoelectric drivers and produce stable dithering at 1 kHz.

10. Three-Micron Region Operation

The FPI can also operate in the 3.2–3.7 μm region. The multilayer dielectric coating has a high-reflectance zone at one-third the design wavelength. This can be seen in Fig. 1, where the reflectance is 0.89 at 3.5 μm . Figure 1 also shows that the width of the reflective zone at 3.5 μm is only one-half as wide as expected from the design calculation. This is probably due to the small deviations from the design thicknesses.

The transmission of the FPI in the 3- μm region is shown in Fig. 7 at two different cavity spacings. As the FPI is scanned through the 8–13 μm region, $n = 2, 3$, and 4 peaks scan through this region. It is possible to collect spectra simultaneously in both the long- and short-wave regions by using a “sandwich” InSb/HgCdTe detector. The InSb detector absorbs the 3- μm band radiation and transmits wavelengths longer than 5.8 μm , which are detected by the HgCdTe. In the dual-band system, a blocking filter of the 5.8–8.2 μm region would be required.

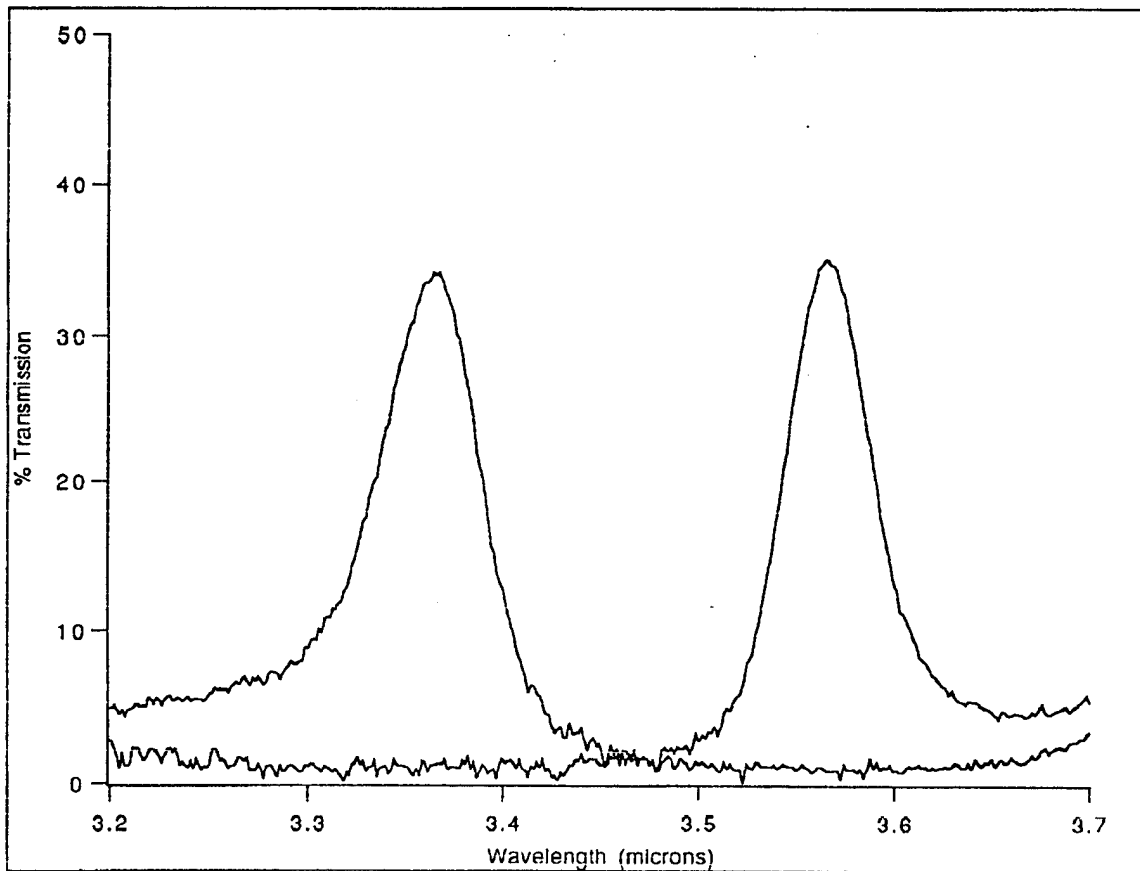


Figure 7. The FPI transmission in the 3- μm region at two cavity spacings.

11. Summary

A scanning, first-order, Fabry–Perot infrared filter has been designed, constructed, and tested. In principle, a first-order FPI can scan from λ_{\max} to $\lambda_{\max}/2$. However, it is difficult to design partially transmitting mirror coatings that cover this large spectral range with uniform reflectivity. The coatings designed for our remote sensing requirements covered the 8.2–12.8 μm range. The wavelength-dependent phase change from the thin-film multilayer dielectric coatings significantly affected the FPI wavelength tuning and transmitted bandwidth. However, these effects are well accounted for by using a model with a fractional, wavelength-dependent order correction. In addition, some loss of the FPI's transmission occurred in the 11–12.8 μm region, probably due to weak absorption by GeO_2 on the mirror coating. Because the filter is electronically tunable, it can provide several unique spectro-metric capabilities. It can scan the full 8.2–12.8 μm range at 20 Hz, or it can dither between smaller spectral regions at rates up to 1 kHz, depending on the spectral interval.

References

1. J. M. Vaughn, *The Fabry-Perot Interferometer*, Adam Higler, Bristol and Philadelphia (1989).
2. M. Born and E. Wolf, *Principles of Optics*, 6th Edition Pergamon Press, NY (1986).
3. P. D. Atherton, N. K. Reay, J. Ring, and T. R. Hicks, *Optical Engineering* **20**, 806 (1981).
4. H. A. MacLeod, *Thin Film Optical Filters*, 2nd Edition, Adam Hilger/McGraw Hill, NY (1986).
5. R. A. Nyquist and R. O. Kagel, *Infrared Spectra of Inorganic Compounds*, Academia Press, NY (1971).
6. Burleigh Instruments, Fishers, NY.

TECHNOLOGY OPERATIONS

The Aerospace Corporation functions as an "architect-engineer" for national security programs, specializing in advanced military space systems. The Corporation's Technology Operations supports the effective and timely development and operation of national security systems through scientific research and the application of advanced technology. Vital to the success of the Corporation is the technical staff's wide-ranging expertise and its ability to stay abreast of new technological developments and program support issues associated with rapidly evolving space systems. Contributing capabilities are provided by these individual Technology Centers:

Electronics Technology Center: Microelectronics, VLSI reliability, failure analysis, solid-state device physics, compound semiconductors, radiation effects, infrared and CCD detector devices, Micro-Electro-Mechanical Systems (MEMS), and data storage and display technologies; lasers and electro-optics, solid state laser design, micro-optics, optical communications, and fiber optic sensors; atomic frequency standards, applied laser spectroscopy, laser chemistry, atmospheric propagation and beam control, LIDAR/LADAR remote sensing; solar cell and array testing and evaluation, battery electrochemistry, battery testing and evaluation.

Mechanics and Materials Technology Center: Evaluation and characterization of new materials: metals, alloys, ceramics, polymers and their composites, and new forms of carbon; development and analysis of thin films and deposition techniques; nondestructive evaluation, component failure analysis and reliability; fracture mechanics and stress corrosion; development and evaluation of hardened components; analysis and evaluation of materials at cryogenic and elevated temperatures; launch vehicle and reentry fluid mechanics, heat transfer and flight dynamics; chemical and electric propulsion; spacecraft structural mechanics, spacecraft survivability and vulnerability assessment; contamination, thermal and structural control; high temperature thermomechanics, gas kinetics and radiation; lubrication and surface phenomena.

Space and Environment Technology Center: Magnetospheric, auroral and cosmic ray physics, wave-particle interactions, magnetospheric plasma waves; atmospheric and ionospheric physics, density and composition of the upper atmosphere, remote sensing using atmospheric radiation; solar physics, infrared astronomy, infrared signature analysis; effects of solar activity, magnetic storms and nuclear explosions on the earth's atmosphere, ionosphere and magnetosphere; effects of electromagnetic and particulate radiations on space systems; space instrumentation; propellant chemistry, chemical dynamics, environmental chemistry, trace detection; atmospheric chemical reactions, atmospheric optics, light scattering, state-specific chemical reactions and radiative signatures of missile plumes, and sensor out-of-field-of-view rejection.